Supporting information for

In Situ Alloying Reaction Constructing Rich Magnesophilic Sites Toward Highly Stable and High-Rate Rechargeable Magnesium Batteries

Haokai Xie, Zihao Ge, Min Zhang, Yan Xin, Shuwei Wang and Huajun Tian**

H. Xie, Z. Ge, M. Zhang, Y. Xin, S. Wang, H. Tian,

Beijing Laboratory of New Energy Storage Technology and Key Laboratory of Power Station Energy Transfer Conversion and System of Ministry of Education

School of Energy Power and Mechanical Engineering

North China Electric Power University

Beijing 102206, China

E-mail: xinyan@ncepu.edu.cn; Huajun.Tian@ncepu.edu.cn

Experimental

Preparation of Bi@Mg anode and Mo_6S_8 cathode

Bi metal particles were evaporated onto 10 cm ×10 cm magnesium (Mg) foil by thermal evaporation under a vacuum of 1–2×10^{-5} Pa using a metal-organic vacuum evaporation system. The resulting Bi-coated Mg foil was cut into 1 cm × 1 cm size to obtain Bi@Mg anodes. The Bi layer thickness was controlled by adjusting the evaporation time, and electrodes with Bi coatings of various thicknesses (0.6–1.2 μm) were prepared, denoted as $Bi_{0.6\mu m}$@Mg, $Bi_{0.8\mu m}$@Mg, $Bi_{1.0\mu m}$@Mg and $Bi_{1.2\mu m}$@Mg, respectively. And the anode with optimized performance was selected and denoted as Bi@Mg. Mg, Al, In, Pb, and Mn coatings were also evaporated onto Mg foil, denoted as Mg@Mg, Al@Mg, In@Mg, Pb@Mg, and Mn@Mg, respectively. Bi coating was evaporated onto Cu foil, denoted as Bi@Cu.

The Mo_6S_8 cathode material was synthesized through a two-step route. Cu (1.288 g, Aladdin, 99.9%), MoS_2 (5.224 g, Aladdin, 99.5%), and Mo (1.522 g, Aladdin, 99.9%) powders were mechanically milled at 480 rpm for 6 h under argon atmosphere using a planetary ball mill. The prepared precursor powders were then annealed at 1000 °C for 24 h under a flowing argon atmosphere (100 mL min^{-1}). The obtained $Cu_2Mo_6S_8$ precursor was acid-leached in 20% hydrochloric acid (HCl) under vigorous stirring for 12 h in air to remove Cu^{2+} ion, washed repeatedly with deionized water, and vacuum-dried at 80 °C for 12 h to yield phase-pure Mo_6S_8. The mixture of Mo_6S_8, polyvinylidene difluoride (PVDF), and Super P (7:2:1) was dissolved in N-methyl-2-pyrrolidone (NMP) to create a slurry. The slurry was subsequently coated onto carbon paper (1 cm × 1 cm) and dried at 80 °C for 12 h in a vacuum to prepare the cathodes. For most cathodes, the Mo_6S_8 active mass loading was in the range of 1–2 mg cm^{-2}. Additionally, cathodes with high active mass loadings of 7–9 mg cm^{-2} were also fabricated.

The electrolyte with 0.4 M $(PhMgCl)_2$-$AlCl_3$ in tetrahydrofuran (THF) (called APC electrolyte) was obtained by dissolving the predetermined amount of PhMgCl/THF and $AlCl_3$ in THF under stirring for at least 24 h.

Materials characterizations

The morphology and compositions were characterized by scanning electron microscopy (SEM, Hitachi S4800) with energy-dispersive spectroscopy (EDS, Oxford EMAX). X-ray diffraction (XRD,

Rigaku Ultima IV, Cu Kα radiation source) was employed for phase structure analysis. Surface roughness and topography were characterized by atomic force microscopy (AFM, Bruker Dimension Icon), and wettability of electrodes was evaluated through contact angle tests via a drop shape analyzer (DSA25S, KRUSS). In situ optical imaging of Mg deposition/stripping was acquired utilizing an optical microscope (YM730TR, Suzhou Yuescope) at a current density of 3.0 mA cm^{-2}. Particle size distribution was tested using a laser particle size analyzer (FRITSCH ANALYSETTE 22NeXT).

Electrochemical characterizations

Electrochemical measurements were carried out using CR2032 coin-type cells assembled in an argon-filled glove box (Vigor, <0.1 ppm O_2 and H_2O) at room temperature. Glass fibers (GF/D, Whatman) separators and 170 μL APC electrolyte were used unless otherwise specified. Symmetric cells were assembled using bare Mg or Bi@Mg electrodes to study the Mg deposition behavior. Asymmetric cells were assembled with titanium (Ti) foil as the cathode and bare Mg or Bi@Mg as the anodes to investigate the CE, with a cut-off voltage of 1.0 V per cycle. Full cells employing the prepared Mo_6S_8 cathode were used to investigate capacity, rate performance, and long-term cycling stability, operating within a voltage range of 0.2–2.0 V. Galvanostatic charge-discharge (GCD) tests were performed using a Land CT3002A battery tester (Wuhan, China). Cyclic voltammetry (CV), electrochemical impedance spectroscopy (EIS) and Tafel curves were conducted on an electrochemical workstation (PARSTAT MC, America). CV curves were recorded in the voltage range of 0.2–2.0 V at scan rates of 0.1–1.0 mV s^{-1}. EIS spectra were measured from 100 kHz to 0.01 Hz with a potential amplitude of 5 mV. Tafel plots were obtained within a potential range of -0.2 to 2.0 V using a scan rate of 1.0 mV s^{-1}. Full-cell tests were performed between 0.2 and 2.0 V, with rate capability evaluated from 0.1 to 5.0 C (1 C = 128 mA g^{-1}) and long-term cycling carried out at 0.2 and 1.0 C. The full cells were activated with three cycles at 0.2 C before long-term cycling at 1 C. Pouch cells employing Bi@Mg‖Mo_6S_8 were also fabricated using APC electrolyte and tested after activation. Pouch cells were fabricated with a 7.6 cm × 6.1 cm Bi@Mg anode, a 7.4 cm × 5.9 cm Mo_6S_8 cathode (Mo_6S_8 loading of 2.12 mg cm^{-2}), and a GF separator to assess practicality using APC electrolyte. The pouch cells were activated with five cycles at 0.1 C before long-term cycling at 1 C within a voltage range of 0.4–2.0 V.

Computational details

All density functional theory (DFT) calculations were performed using the Vienna Ab initio Simulation Package (VASP, version 6.3.2).[1,2] The exchange-correlation energy was treated within the generalized gradient approximation (GGA) using the Perdew-Burke-Ernzerhof (PBE) functional.[3] Electron-ion interactions were described by the projector augmented wave (PAW) method using the corresponding pseudopotentials.[4] Based on the most intense diffraction peaks in the XRD patterns, the Mg (002), Bi (003), Mg_3Bi_2 (011) and Mg_3Bi_2 (002) crystal planes were selected for the computational modeling. 3×3×1 broad cells were performed on the all types. Meanwhile, after the cell expansion, all models were assigned a 25 Å vacuum layer to ensure that the atoms had sufficient relaxation space. A 5×5×2 Monkhorst-Pack k-point grid was employed in the crystal structure optimization process, with a plane wave cutoff energy of 500 eV. All lattice parameters and ionic positions were fully relaxed until the total energy and forces reached convergence criteria of 10^{-6} eV and 0.03 eV $Å^{-1}$, respectively.

In addition, the diffusion kinetics of Mg atom were studied by the climbing-image nudged elastic band (Cl-NEB) method. Firstly, the initial and final state structures of Mg on the Mg, Bi and Mg_3Bi_2 surfaces were fully optimized. Subsequently, by inserting five intermediate states into the reactants and products, linear interpolation was performed on the optimized initial and final state structures to obtain the minimum activation energy of the reaction.

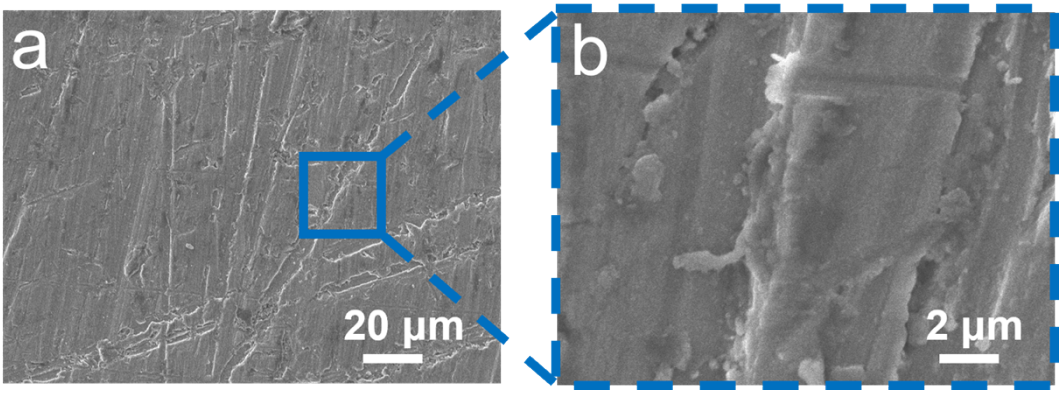

Figure S1. Top-view SEM images of the polished Mg foil.

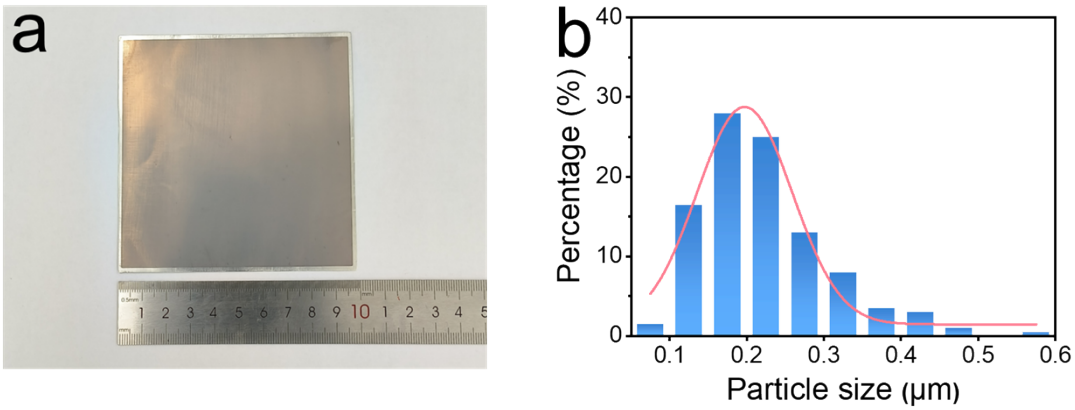

Figure S2. (a) Photograph of Bi-coated Mg foil (size ~ 10 cm × 10 cm); (b) Histograms of Bi metal particle size distribution.

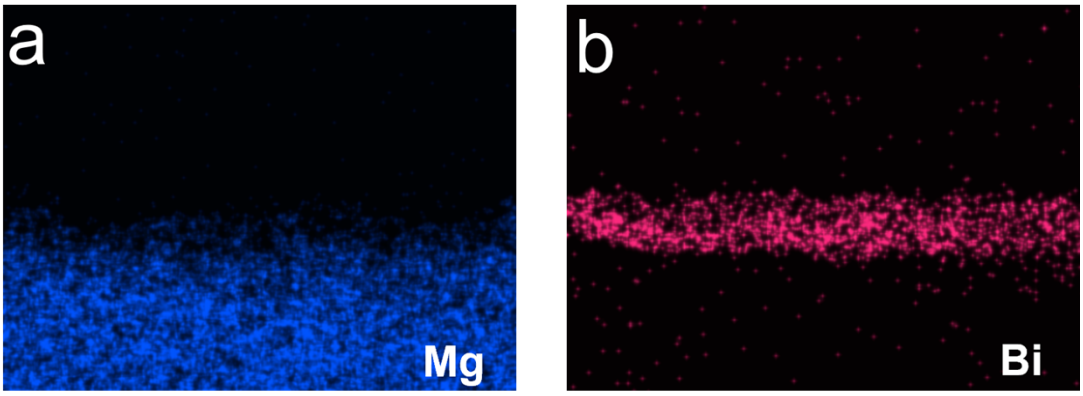

Figure S3. Cross-sectional EDS mappings for Bi@Mg anode.

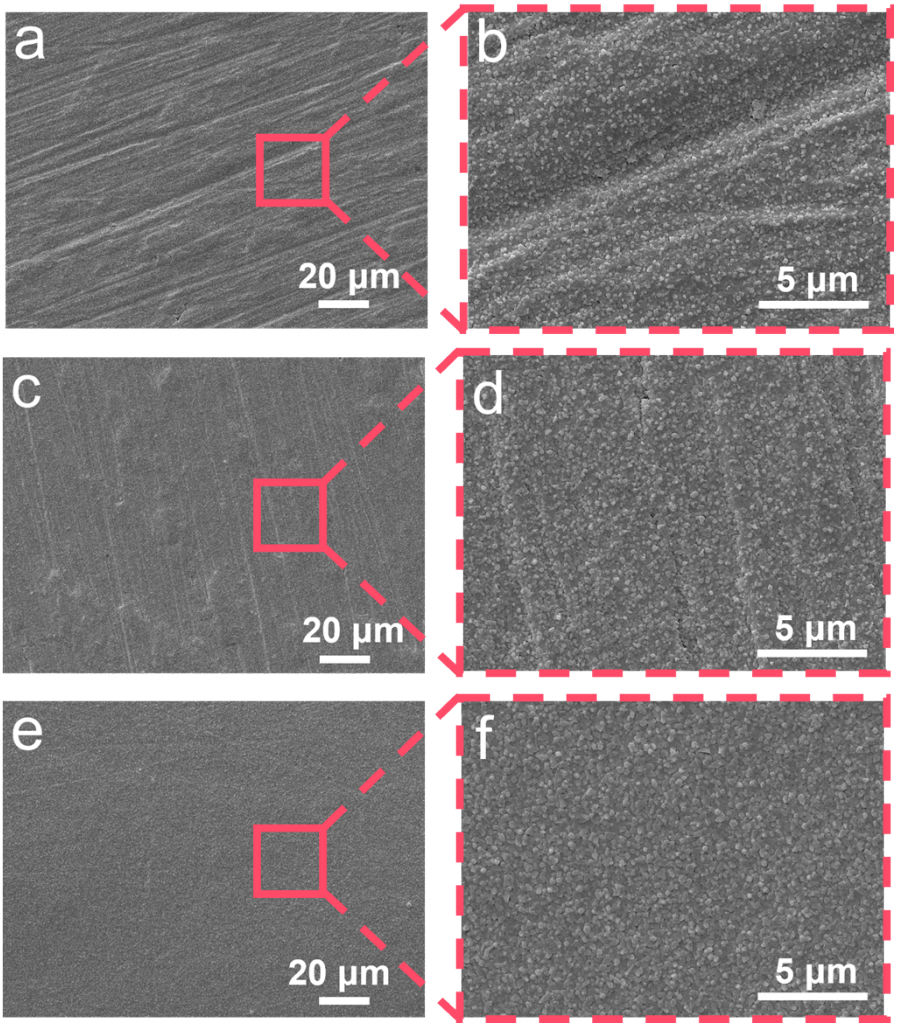

Figure S4. Top-view SEM images of the Bi@Mg anodes with Bi metal layer of (a,b) 0.6 μm; (c,d) 0.8 μm; (e,f) 1.2 μm thickness.

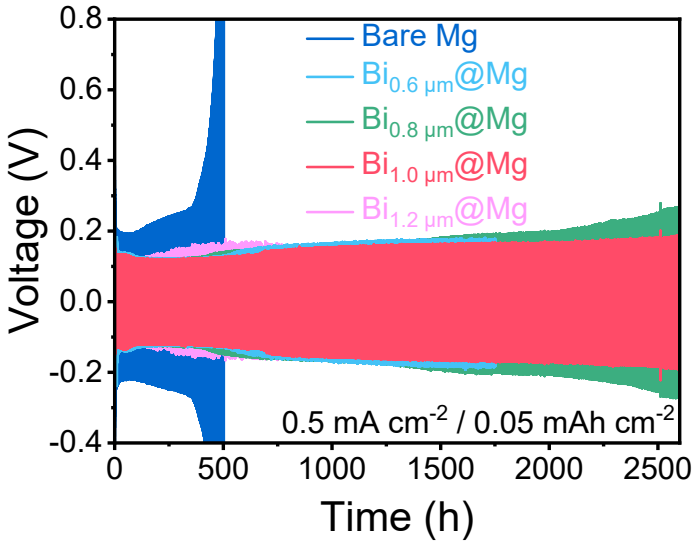

Figure S5. Charge-discharge curves of symmetric cells with varying Bi metal layer thicknesses (0.6, 0.8, 1.0, and 1.2 μm for $Bi_{0.6\ \mu m}$@Mg, $Bi_{0.8\ \mu m}$@Mg, $Bi_{1.0\ \mu m}$@Mg and $Bi_{1.2\ \mu m}$@Mg, respectively) at a current density of 0.5 mA cm^{-2} (areal capacity: 0.05 mAh cm^{-2}).

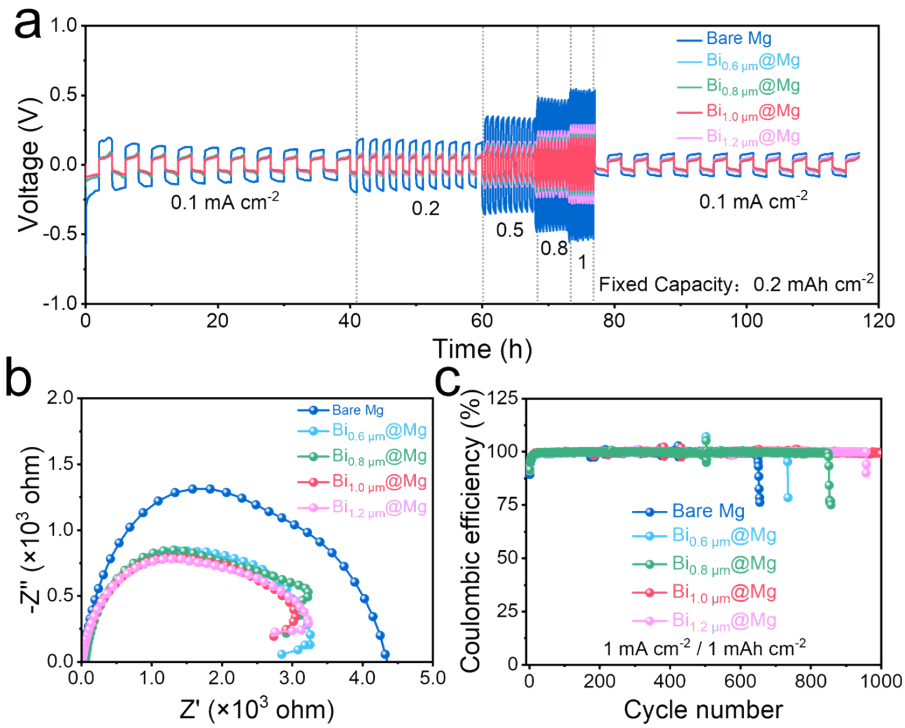

Figure S6. (a) Rate capability, (b) Nyquist plots of symmetric cells, and (c) long-term cycling performance of asymmetric cells for anodes with varying Bi metal layer thickness.

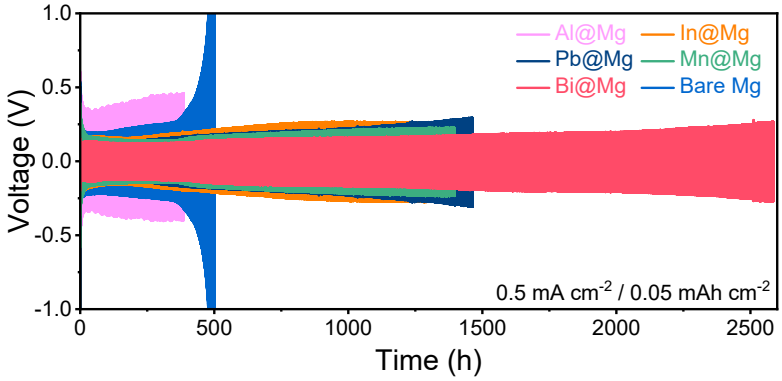

Figure S7. GCD curves of symmetric cells based on Mg metal anodes coated with different metal layers.

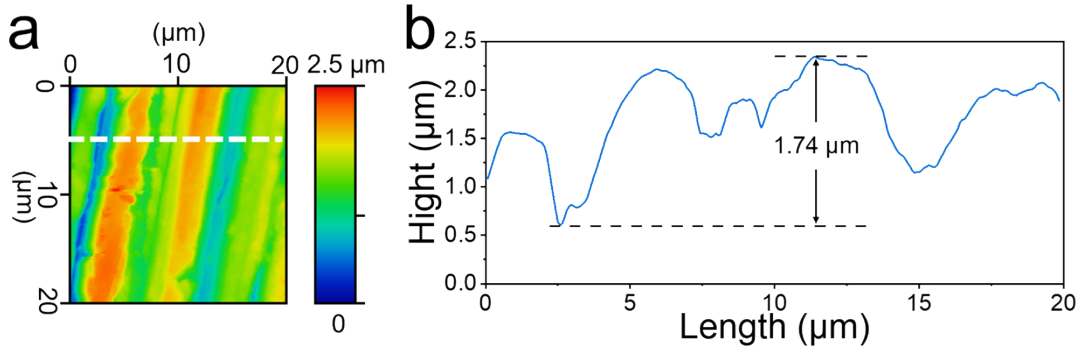

Figure S8. (a) 2D AFM image of bare Mg and (b) height profile along the marked dotted line.

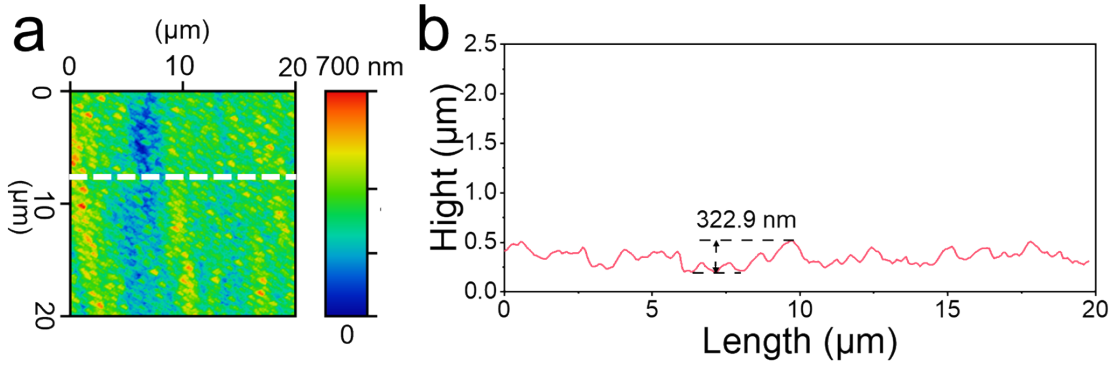

Figure S9. (a) 2D AFM image of Bi@Mg and (b) height profile along the marked dotted line.

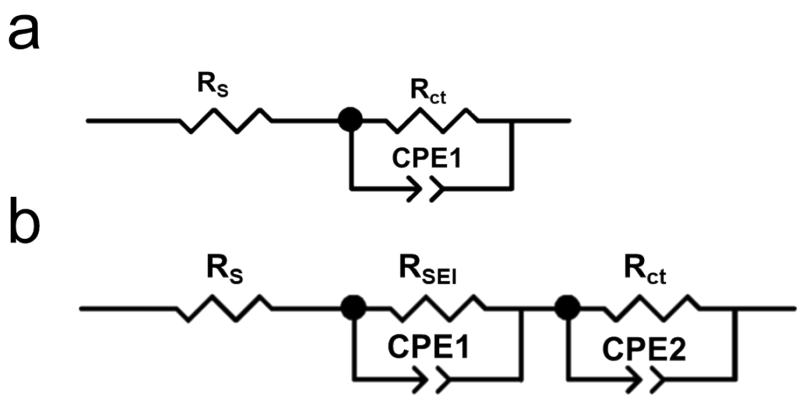

Figure S10. Equivalent circuits used for fitting impedance behavior of the (a) bare Mg and (b) Bi@Mg anodes. R_s is the bulk resistance of system. R_{ct} is the interfacial charge transfer resistance. R_{SEI} is the SEI resistance. CPE1 and CPE2 are the corresponding constant phase elements.

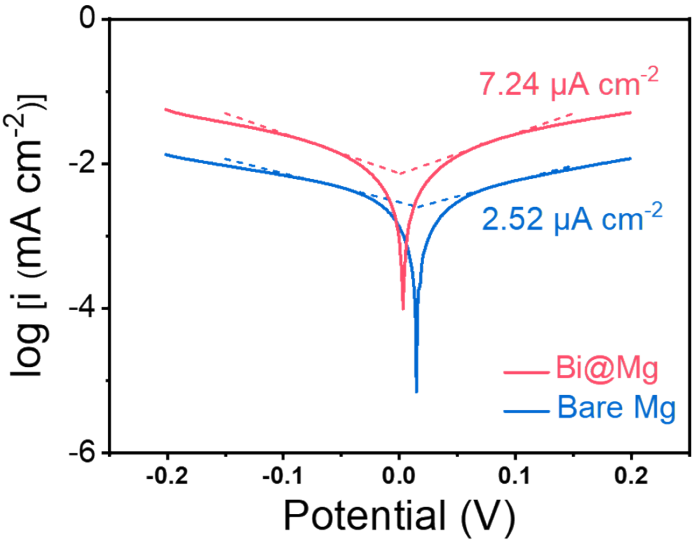

Figure S11. Tafel plots of symmetric cells with bare Mg and Bi@Mg anodes.

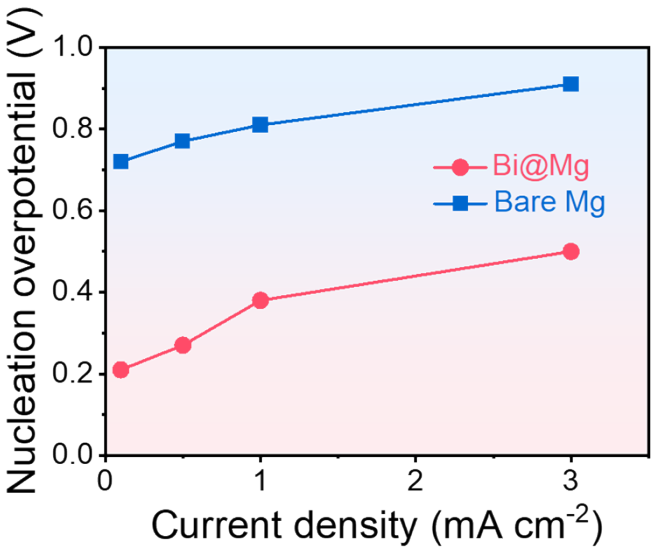

Figure S12. Relationship between NOP and current density corresponding to **Figure 2e–f**.

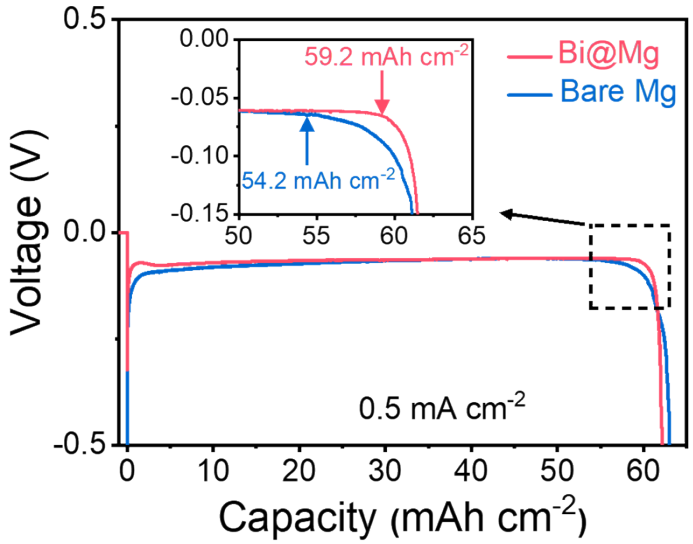

Figure S13. Single galvanostatic plating curves of bare Mg||bare Mg and Bi@Mg||Bi@Mg symmetric cells.

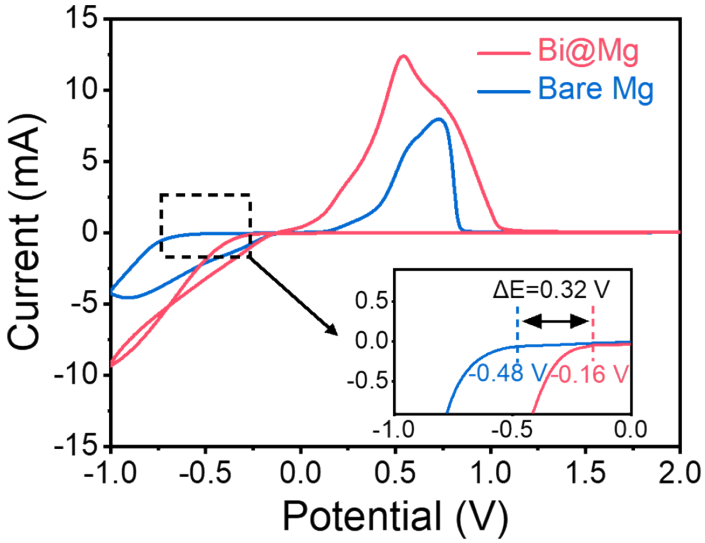

Figure S14. CV curves of bare Mg||Ti and Bi@Mg||Ti asymmetric cells at 10 mV s^{-1}.

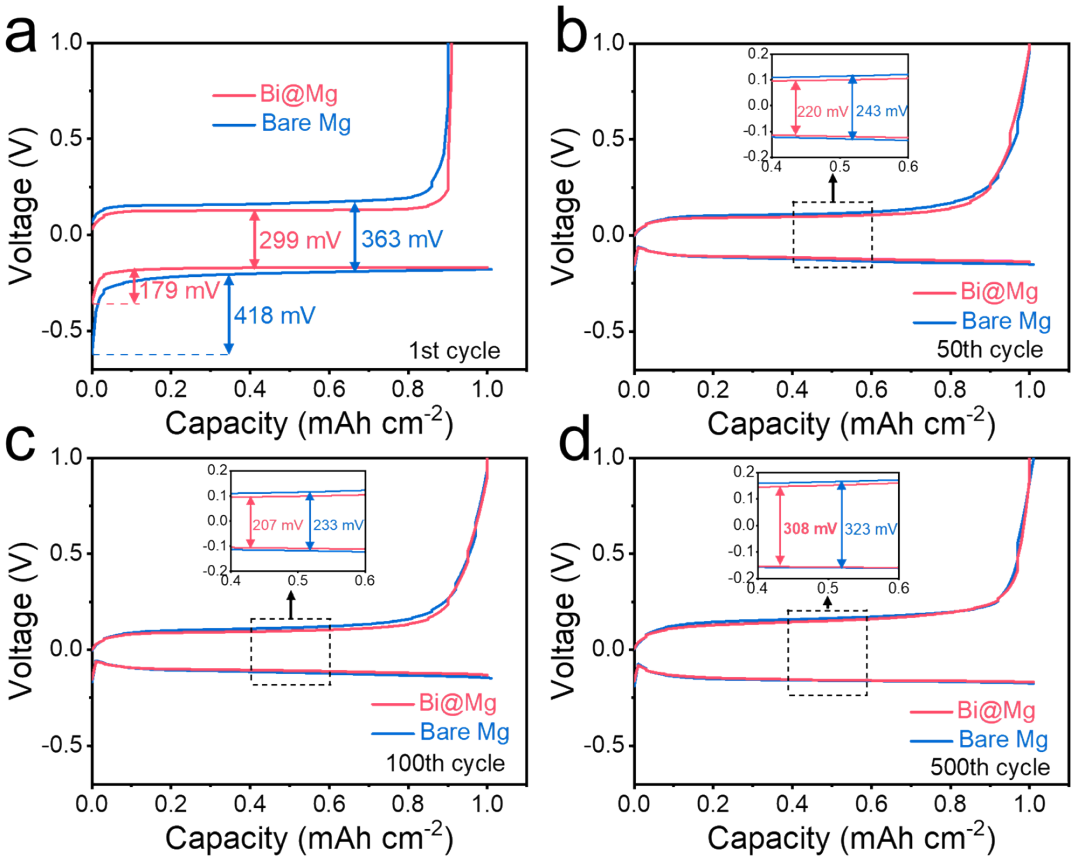

Figure S15. The GCD profiles of the asymmetrical cells at different cycles**.** (a)1st cycle; (2) 50th cycle; (c) 100th cycle; (d) 500th cycle.

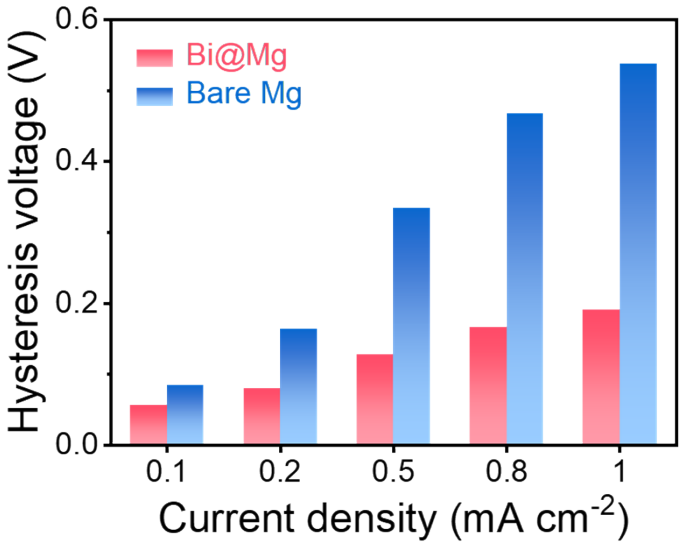

Figure S16. Corresponding hysteresis voltage at different current densities in **Figure 3b**.

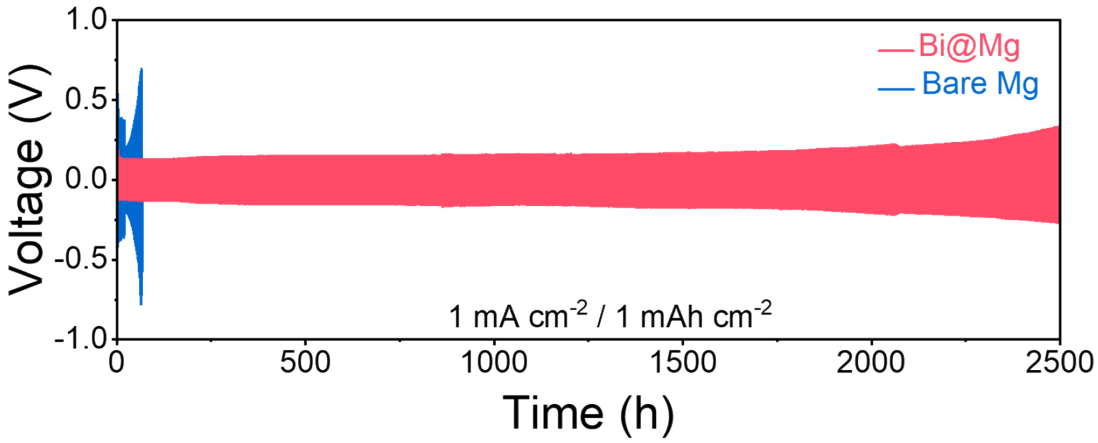

Figure S17. Galvanostatic curves of Mg||Mg and Bi@Mg||Bi@Mg symmetric cells at 1 mA cm^{-2} (areal capacity: 1 mAh cm^{-2}).

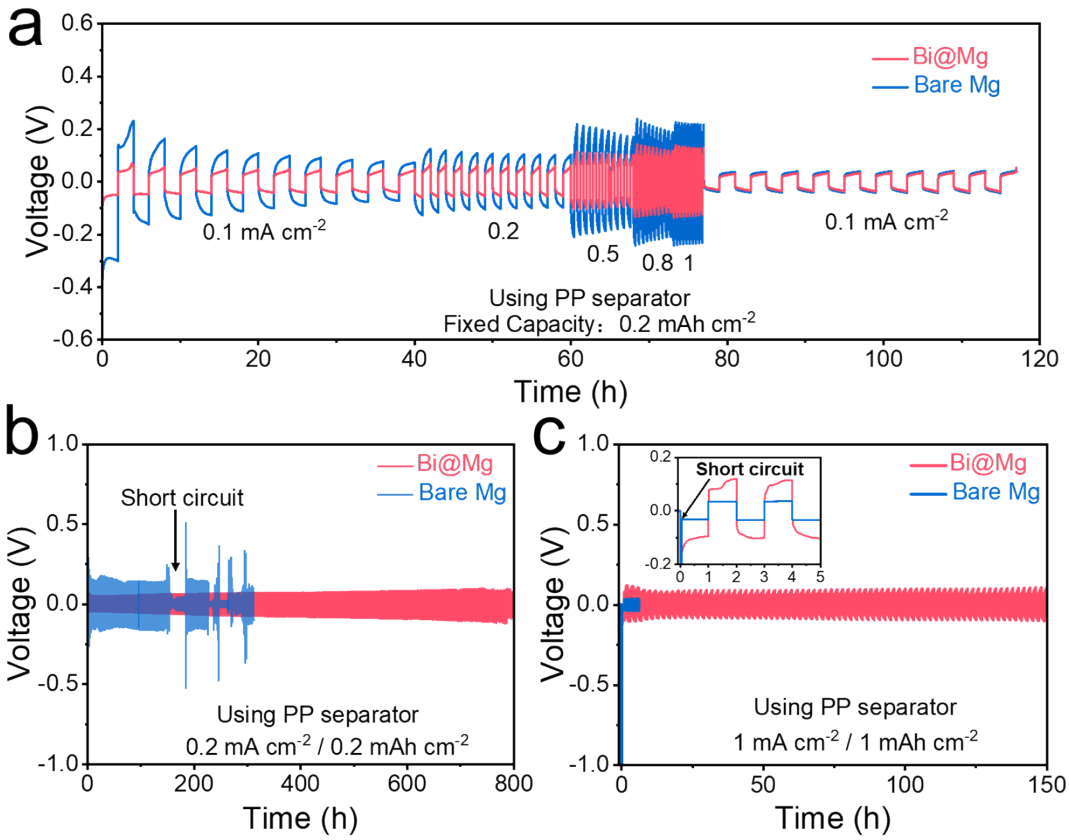

Figure S18. Symmetric cell performance with a PP separator. (a) The rate capability under 0.1 to 1.0 mA cm^{-2} (fixed areal capacity:0.2 mAh cm^{-2}); Cycling performance at (b) 0.2 mA cm^{-2} (areal capacity: 0.2 mAh cm^{-2}) and (c) 1 mA cm^{-2} (areal capacity: 1 mAh cm^{-2});

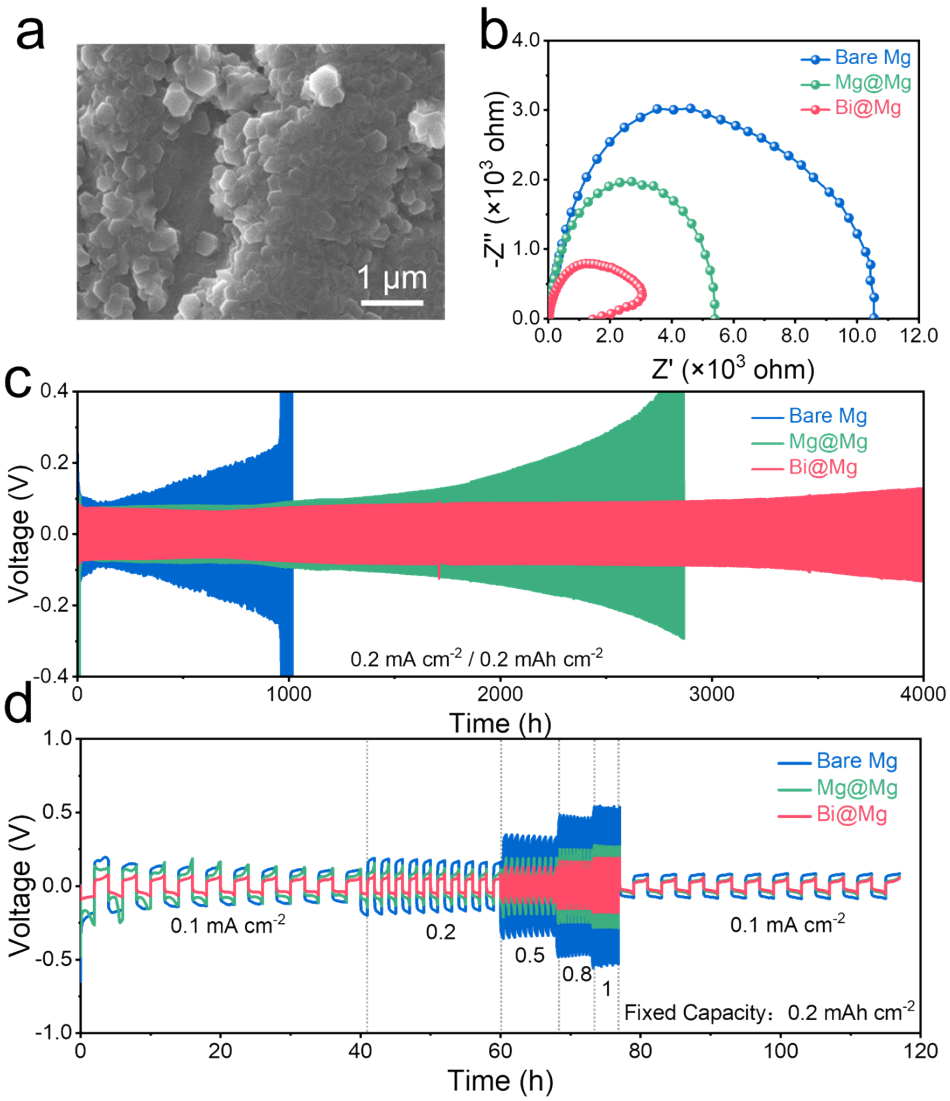

Figure S19. (a) SEM image of the Mg@Mg anode. (b) Nyquist plots of the bare Mg||bare Mg, Mg@Mg||Mg@Mg, and Bi@Mg||Bi@Mg symmetric cells. (c) Galvanostatic charge/discharge curves of symmetric cells at 0.2 mA cm^{-2} (area capacity: 0.2 mAh cm^{-2}). (d) Rate capability of symmetric cells tested from 0.1 to 1.0 mA cm^{-2}.

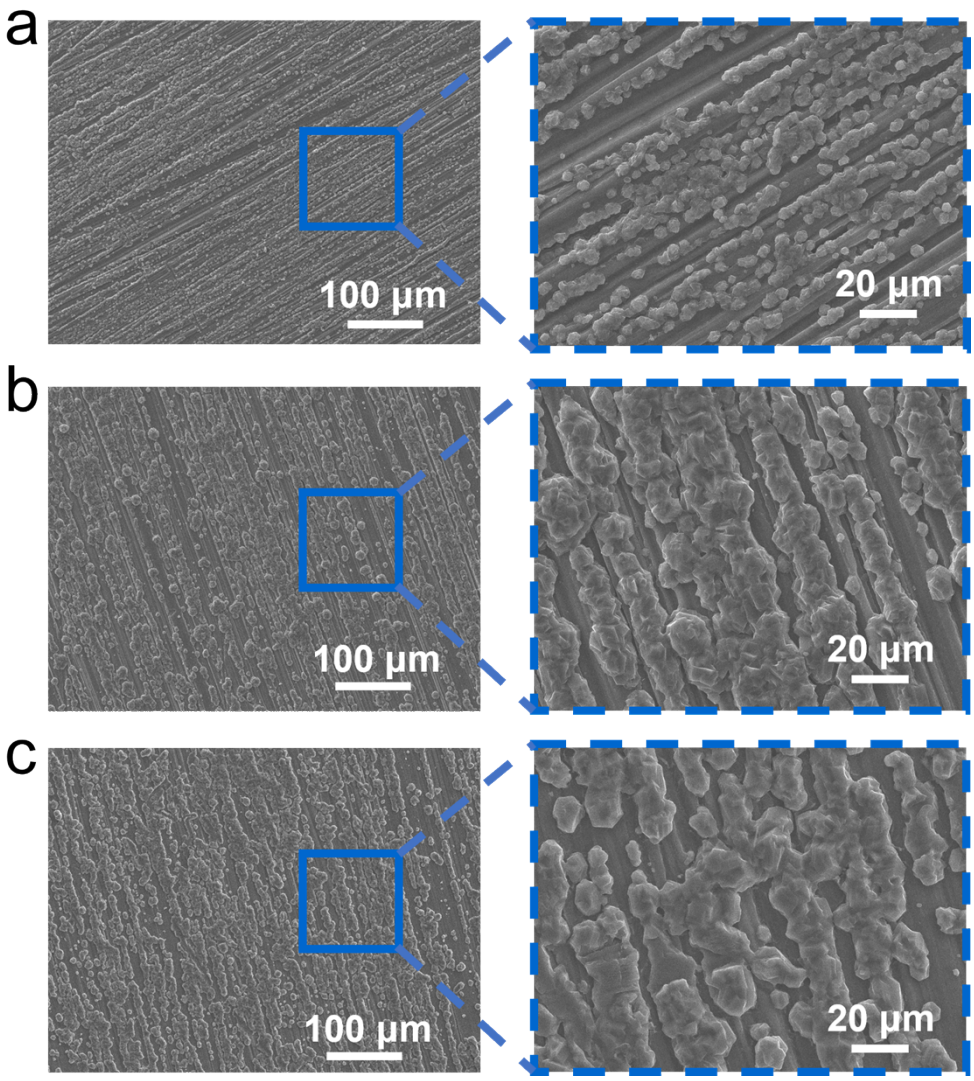

Figure S20. SEM images of bare Mg anodes in symmetric cells after Mg plating at 1 mA cm^{-2} with capacity of (a) 1, (b) 2 and (c) 3 mAh cm^{-2}.

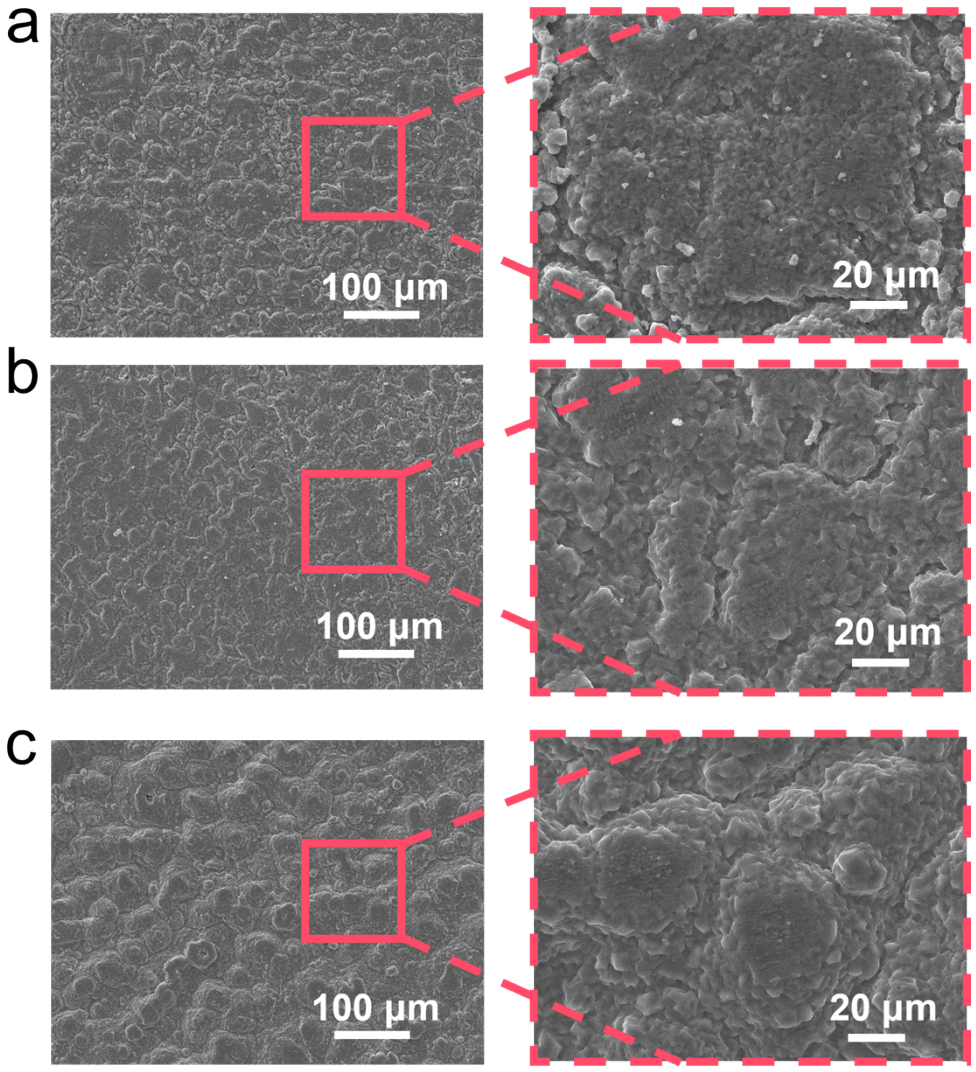

Figure S21. SEM images of Bi@Mg anodes in symmetric cells after Mg plating at 1 mA cm^{-2} with capacity of (a) 1, (b) 2 and (c) 3 mAh cm^{-2}.

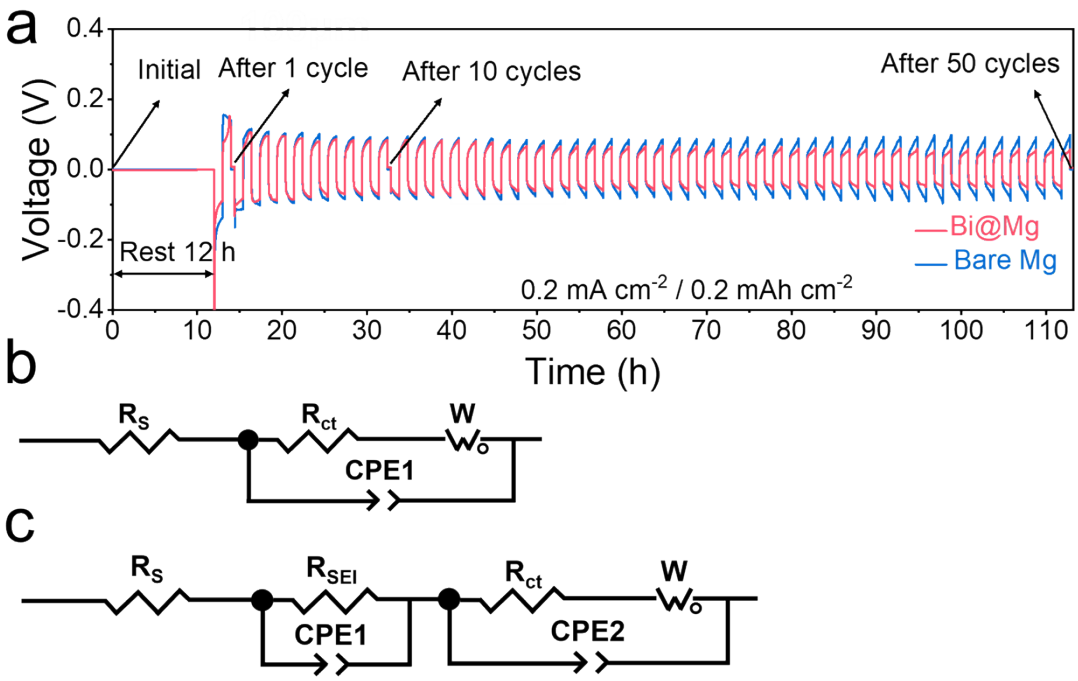

Figure S22. (a) GCD curves of symmetric Mg||Mg cell and Bi@Mg||Bi@Mg cells at 0.2 mA cm^{-2} (areal capacity: 0.2 mAh cm^{-2}) during in-situ EIS testing; Equivalent circuits used for fitting impedance behavior of the (b) bare Mg and (c) Bi@Mg anodes.

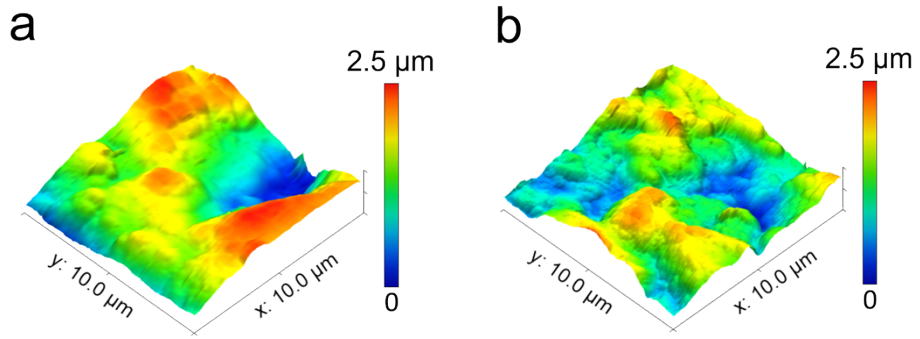

Figure S23. AFM images of (a) bare Mg and (b) Bi@Mg electrodes from symmetric cells after 10 cycles at 0.2 mA cm^{-2} (area capacity: 0.2 mAh cm^{-2}).

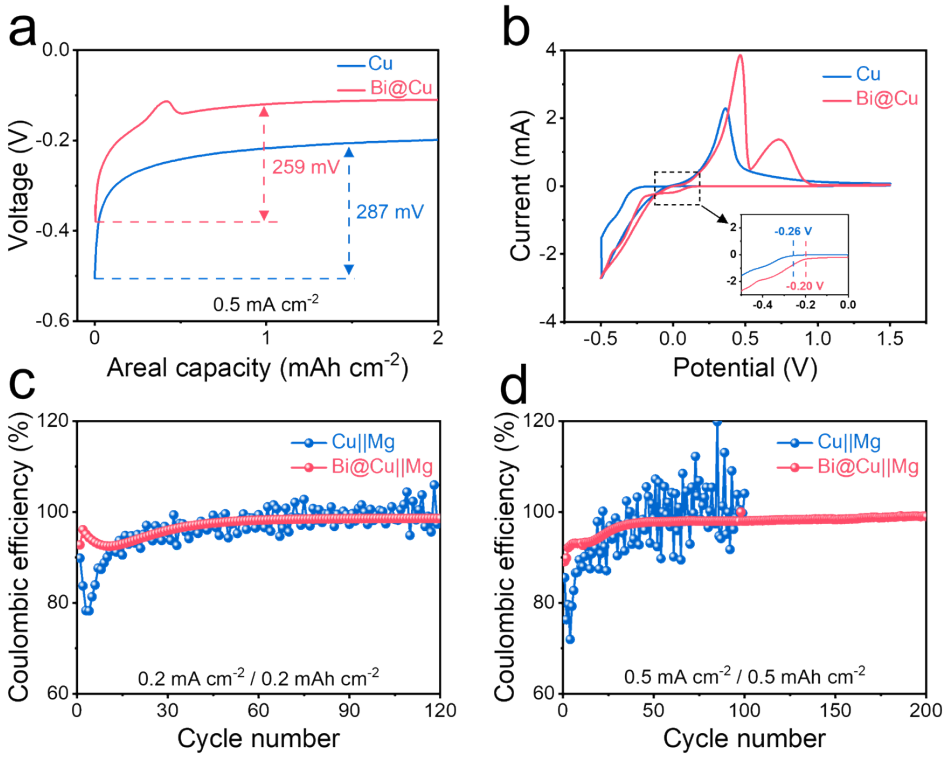

Figure S24. (a) Voltage profiles of Mg deposition on Cu and Bi@Cu electrodes at 0.5 mA cm^{-2}. (b) CV curves of Cu||Mg and Bi@Cu||Mg asymmetric cells at 10 mV s^{-1}. Cycling performance of Cu||Mg and Bi@Cu||Mg asymmetric cells under (c) 0.2 mA cm^{-2} and (d) 0.5 mA cm^{-2}.

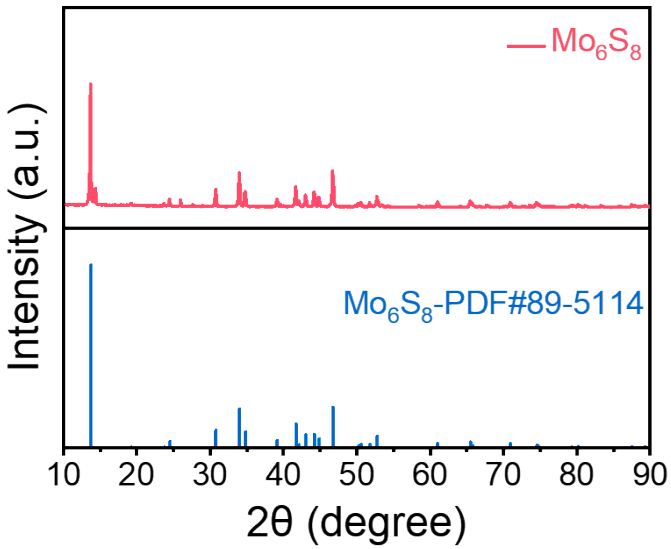

Figure S25. XRD pattern of the synthesized Mo_6S_8 samples.

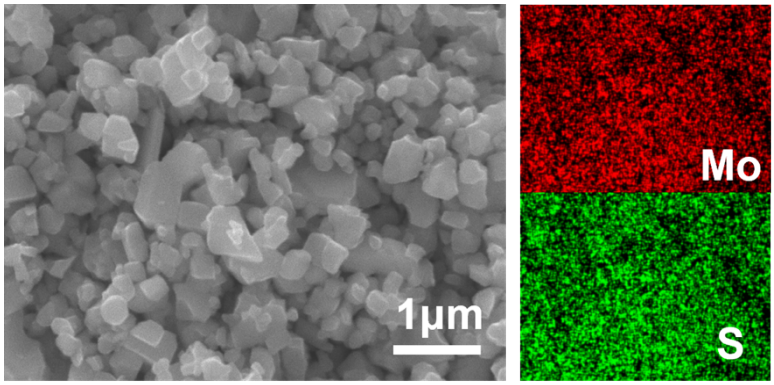

Figure S26. SEM and EDS images of the synthesized Mo_6S_8 samples.

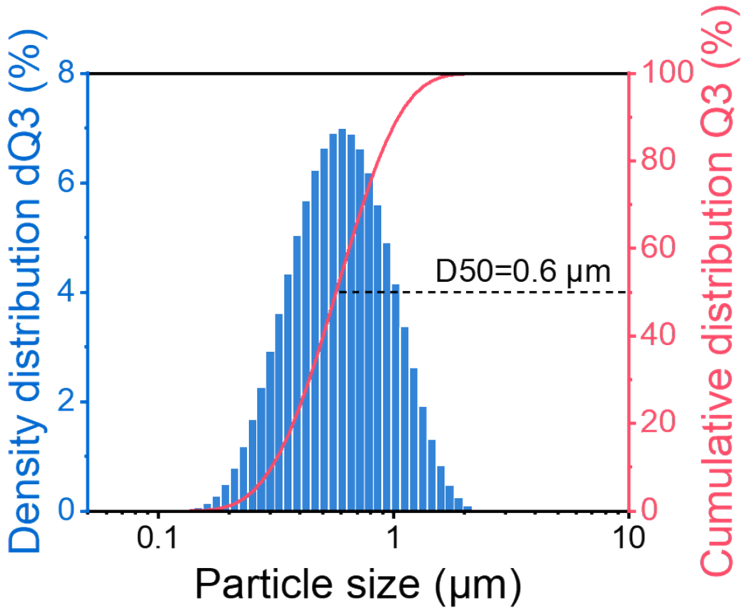

Figure S27. Particle size distribution diagram of the synthesized Mo_6S_8 samples.

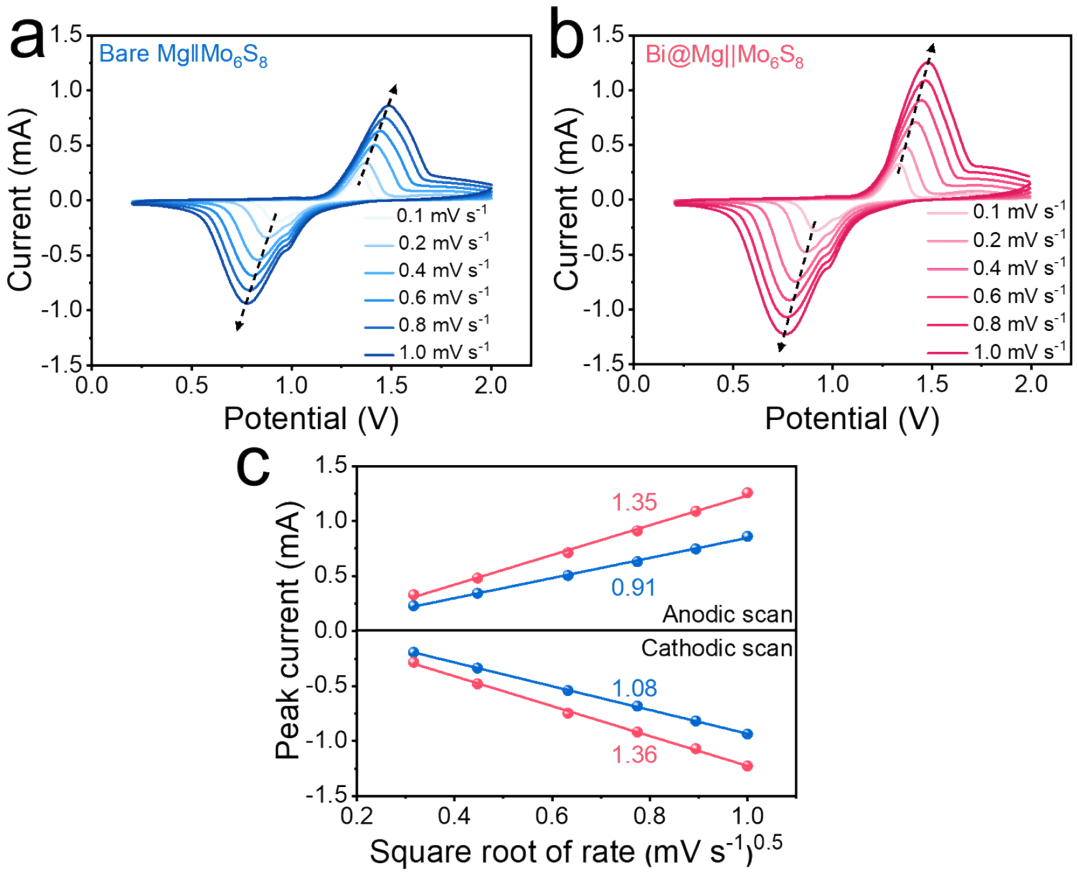

Figure S28. CV curves of (a) bare Mg||Mo_6S_8 and (b) Bi@Mg||Mo_6S_8 full cells at different scan rates from 0.1 to 1.0 mV s^{-1} in the voltage range of 0.2–2.0 V. (c) The square root of scan rate ($v^{0.5}$) of full cells with bare Mg and Bi@Mg anodes.

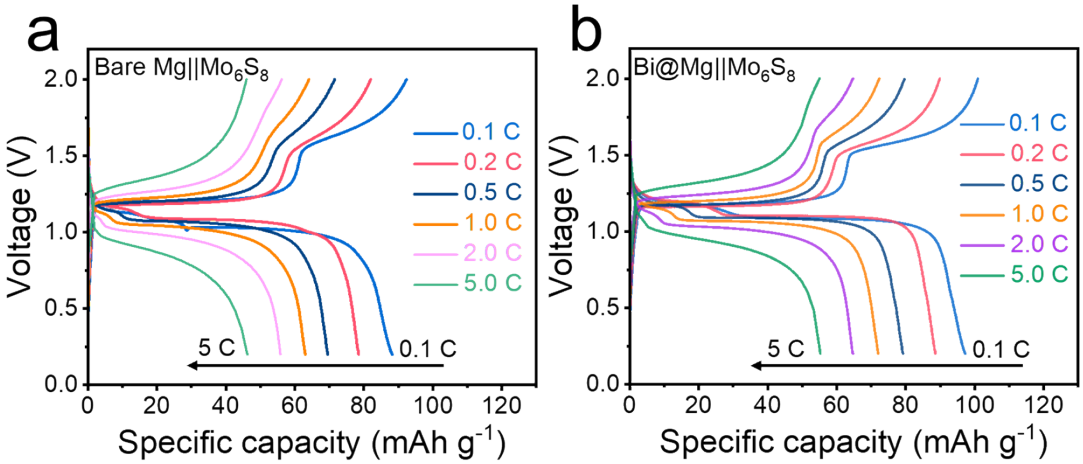

Figure S29. Charge/discharge voltage curves of the (a) bare Mg||Mo_6S_8 and (b) Bi@Mg||Mo_6S_8 full cells at 0.1, 0.2, 0.5, 1.0, 2.0 and 5.0 C.

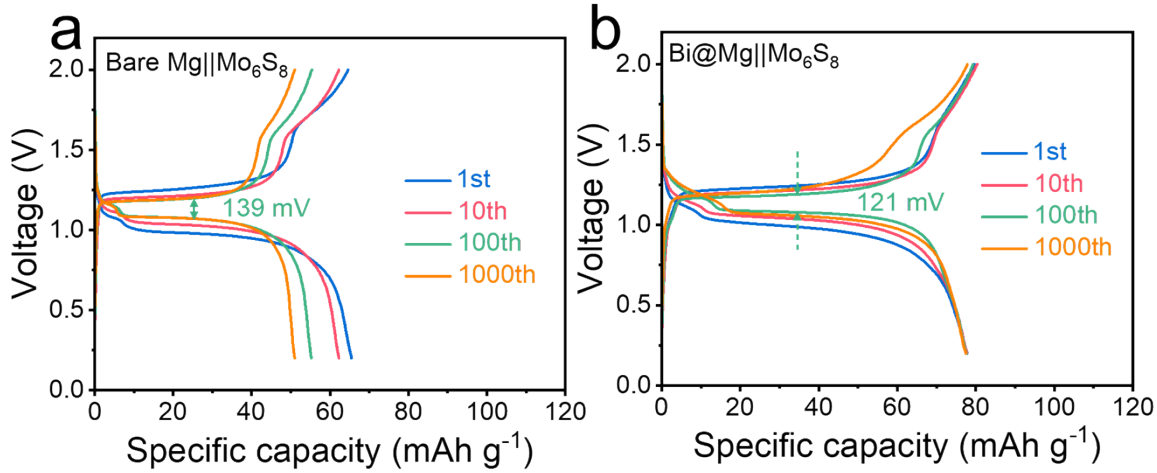

Figure S30. Charge/discharge voltage curves of the (a) bare Mg||Mo_6S_8 and (b) Bi@Mg||Mo_6S_8 full cells at 1 C.

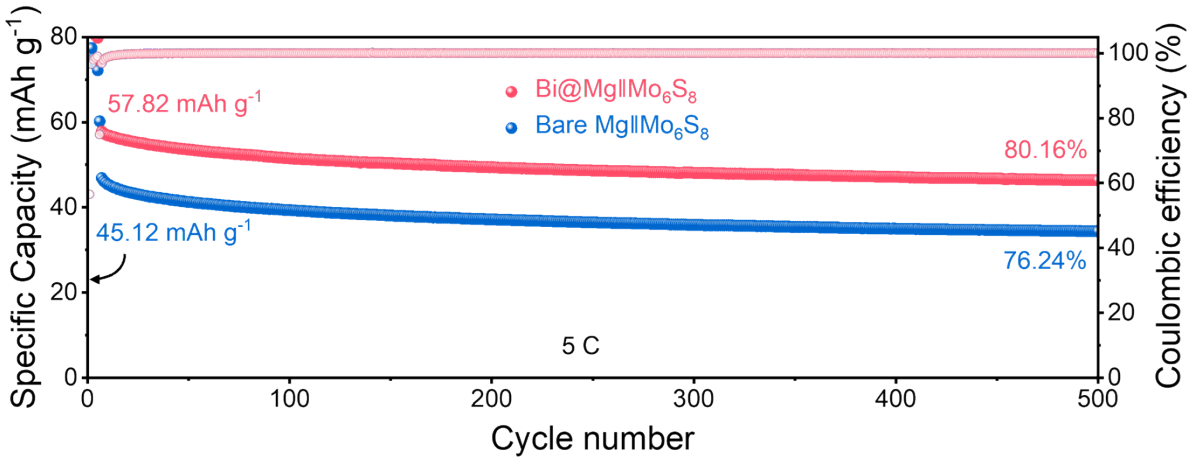

Figure S31. Long-term cycling performance of bare Mg||Mo_6S_8 and Bi@Mg||Mo_6S_8 full cells at a high rate of 5 C.

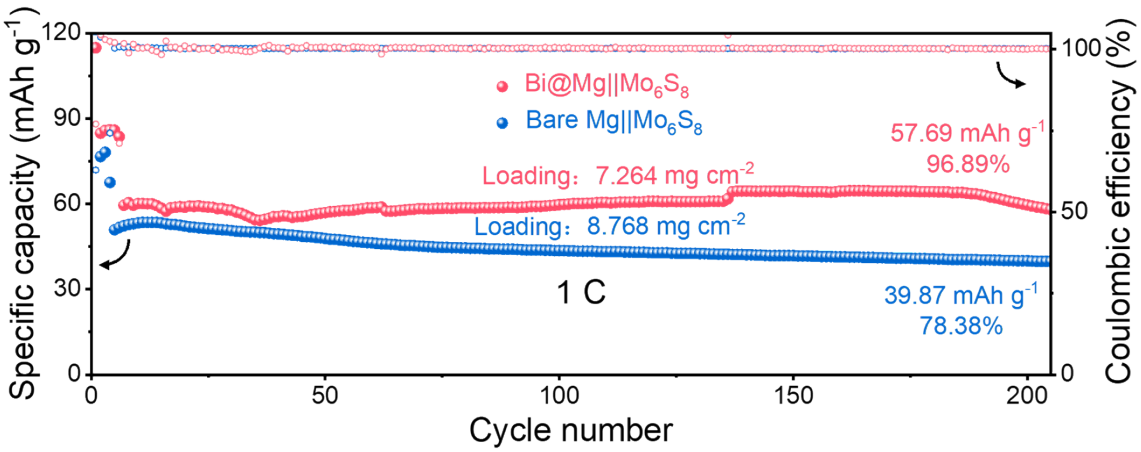

Figure S32. Cycling performance of bare Mg||Mo_6S_8 and Bi@Mg||Mo_6S_8 full cells at 1 C under a high loading (7–9 mg cm^{-2}).

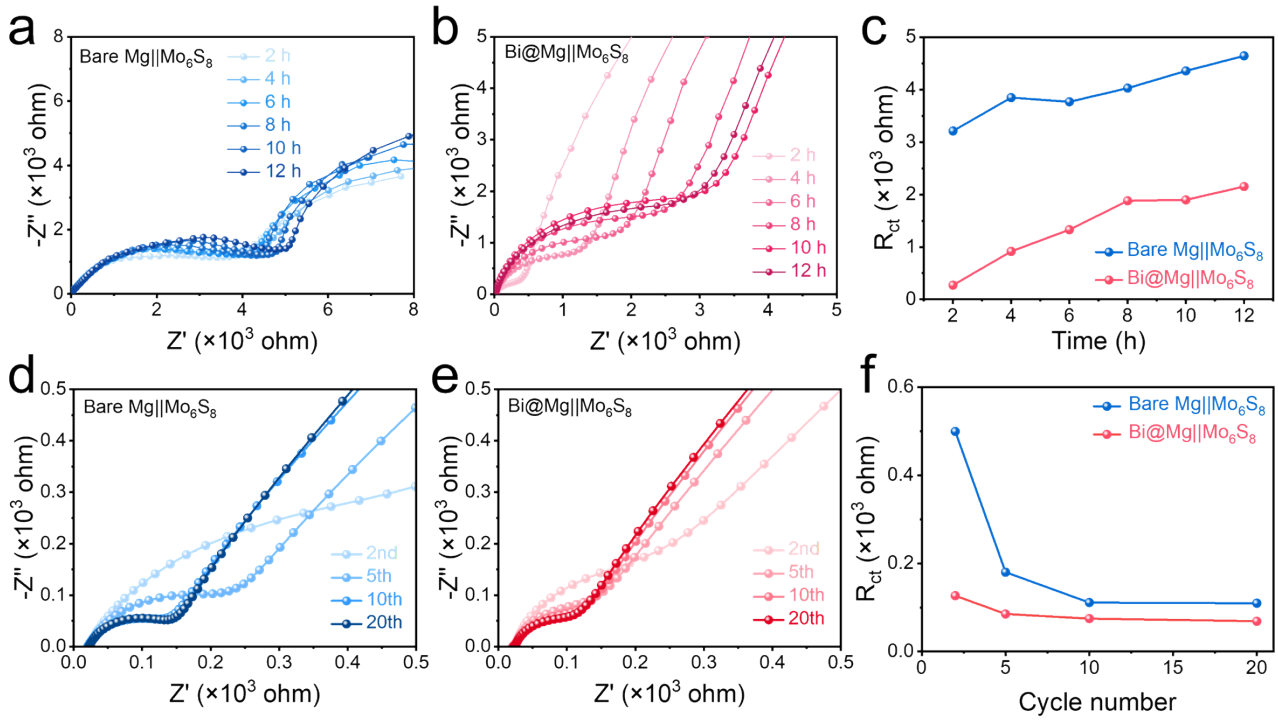

Figure S33. Nyquist plots of the (a) Bare Mg||Mo_6S_8 and (b) Bi@Mg||Mo_6S_8 full cells during the resting time. (c) Variation of the corresponding R_{ct} values with prolonging time. Nyquist plots of the (d) Bare Mg||Mo_6S_8 and (e) Bi@Mg||Mo_6S_8 full cells with cycling. (f) Variation of the corresponding R_{ct} values with cycling.

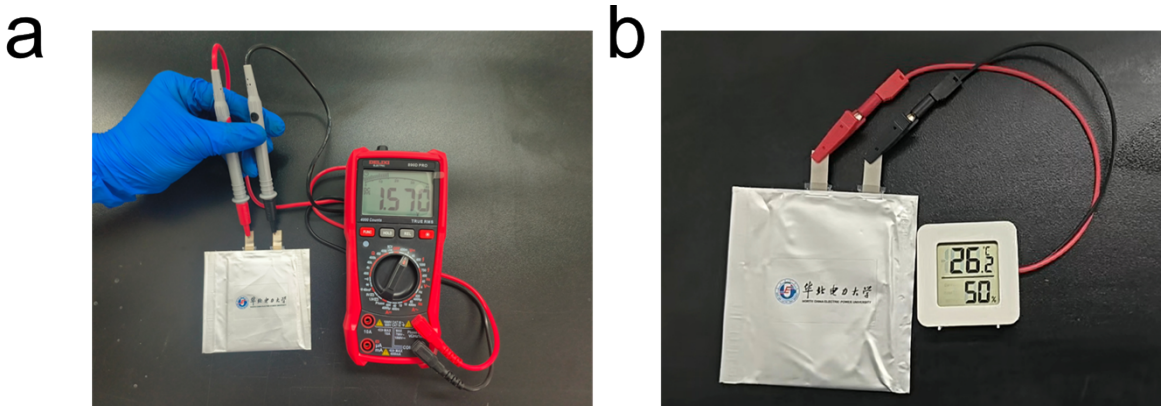

Figure S34. (a) Photograph of the open circuit voltage of a Bi@Mg||Mo_6S_8 pouch cell and (b) the electronic display unit lightened by a Bi@Mg||Mo_6S_8 pouch cell.

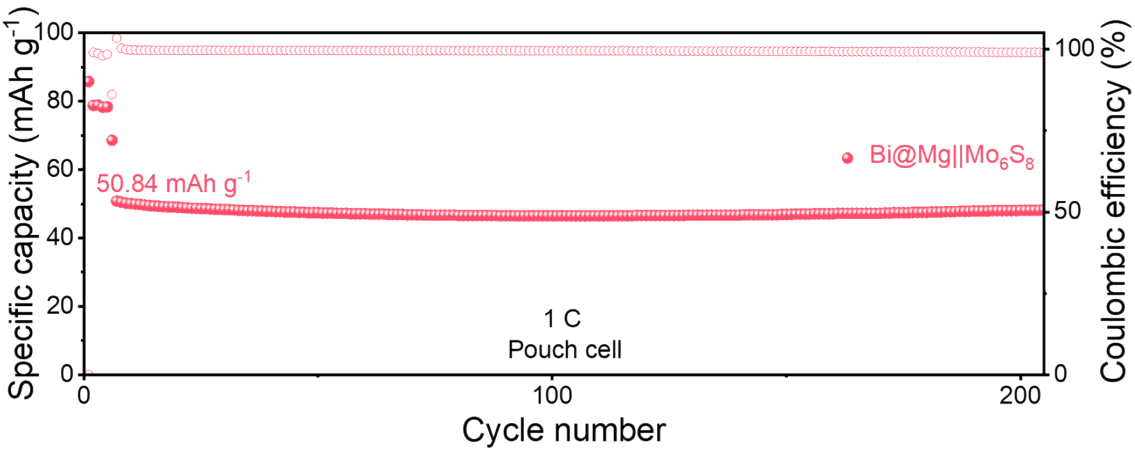

Figure S35. Cycling performance of the Bi@Mg||Mo_6S_8 pouch cell at 1 C.

Table S1. The fitting values of resistances for Mg||Mg symmetric cells with prolonging time.

Samples	R_s (Ω)	Error (%)	R_{ct} (Ω)	Error (%)
Initial	10.08	2.26	2.08×10^4	1.21
2 h	199.00	9.45	3.30×10^4	0.90
4 h	255.70	6.51	6.70×10^4	1.13
6 h	326.30	4.98	1.16×10^5	1.09
8 h	337.10	4.55	1.71×10^5	1.05
10 h	334.90	5.82	2.36×10^5	1.31
12 h	330.00	6.29	3.13×10^5	1.62

Table S2. The fitting values of R_s, R_{SEI} and R_{ct} for Bi@Mg||Bi@Mg symmetric cells with prolonging time.

Samples	R_s (Ω)	Error (%)	R_{SEI} (Ω)	Error	R_{ct} (Ω)	Error (%)
Initial	10.89	0.33	1.97	12.17%	3.38×10^3	0.67
2 h	11.00	0.36	11.01	2.47%	4.47×10^3	0.50
4 h	10.88	0.40	14.39	2.54%	1.27×10^4	0.41
6 h	10.74	0.50	16.33	3.20%	1.64×10^4	0.64
8 h	10.66	0.51	18.88	3.35%	1.84×10^4	0.68
10 h	10.68	0.59	21.01	4.00%	2.03×10^4	0.64
12 h	10.64	0.64	24.46	4.53%	2.09×10^4	0.64

Table S3. A summary of the reported electrochemical performance of modified Mg metal anodes by different artificial interphases.

Electrodes	Thickness (μm)	Electrolyte	Current density (mA cm^{-2})	Capacity (mAh cm^{-2})	Cycling lifespan (h)	Refs.
Mg@SnSb	4.0	$Mg(OTf)_2$/DME	1.0	1.0	1500	5
PA-M@Mg	1.6–1.9	APC	3.0	1.0	2400	6
In/$MgCl_2$@Mg	2.3	APC	1.0	0.5	1800	7
			3.0	1.0	1000	
Mg-Sn-Bi@Mg	1.0	APC	0.2	0.2	1000	8
			0.5	0.05	1400	
Mg-Sn/Bi@Mg	2.2/3.5	APC	0.2	0.2	1000	9
Zn-based@Mg	6.0	0.5 M $Mg(TFSI)_2$/G2	0.1	0.05	1000	10
Sb-based@Mg	5.0	0.5 M $Mg(TFSI)_2$/DME	0.2	0.2	800	11
PA-based@Mg	~1.5	APC	0.2	0.2	2000	12
			3.0	1.0	500	
GPL@Mg	15.0	0.5 M $Mg(TFSI)_2$/DME	0.5	0.5	200	13
Sb-Mg/$MgCl_2$@Mg	1.5	0.3 M $Mg(OTf)_2$+0.2 M $MgCl_2$/DME	1.0	1.0	1200	14
			3.0	3.0	750	
Si-based@Mg	8.0	0.5 M $Mg(TFSI)_2$/DME	0.1	0.05	600	15
			0.1	1.0	1400	
Ge-based@Mg	>2.0	0.5 M $Mg(OTf)_2$+0.4 M $GeCl_2$/DME	10.0	5.0	350	16
$MgCl_2$@Polymer	~2.0	0.5 M $Mg(TFSI)_2$/DME	0.1	0.05	700	17
DES-Mg	20.0	0.5 M $Mg(TFSI)_2$/DME	0.5	2.0	400	18
MBI@Mg	7.5	0.5 M $Mg(TFSI)_2$/DME	1.0	0.5	1750	19
MIEC@Mg	72.4	0.5 M $Mg(TFSI)_2$/DME	6.0	3.0	800	20
FRAB@Mg	20.0	0.5 M $Mg(TFSI)_2$/DME	0.5	0.25	2200	21
Ga_5Mg_2@Mg	4.5	0.5 M $Mg(TFSI)_2$/DME +20 wt%MOIPA	1.0	1.0	500	22
Bi@Mg	1.0	APC	0.2	0.2	4000	**This work**
		APC	0.5	0.05	2700	
		APC	1.0	1.0	2500	

Table S4. The fitting values of R_s and R_{ct} for Mg||Mg symmetric cells after different in situ EIS cycles.

Samples	R_s (Ω)	Error (%)	R_{ct} (Ω)	Error (%)
Initial	12.44	1.13	4.59×10^4	1.26
After 1 cycle	13.41	0.27	5.50×10^3	2.12
After 10 cycles	14.98	0.49	352.40	1.60
After 50 cycles	16.97	0.40	238.50	1.50

Table S5. The fitting values of R_s, R_{SEI} and R_{ct} for Bi@Mg||Bi@Mg symmetric cells after different in situ EIS cycles.

Samples	R_s (Ω)	Error (%)	R_{SEI} (Ω)	Error (%)	R_{ct} (Ω)	Error (%)
Initial	10.62	0.62	6.82	3.43	2.68×10^3	0.56
After 1 cycle	10.96	0.35	8.13	3.93	445.90	0.98
After 10 cycles	11.30	0.38	7.33	3.53	125.60	2.67
After 50 cycles	10.69	0.26	6.62	3.12	68.90	2.06

Table S6. The fitting values of R_s and R_{ct} for bare Mg||Mo_6S_8 and Bi@Mg||Mo_6S_8 full cells.

Samples	R_s (Ω)	Error (%)	R_{ct} (Ω)	Error (%)
Bare Mg//Mo_6S_8	54.40	0.76	5.84×10^3	3.70
Bi@Mg//Mo_6S_8	10.82	0.28	712.80	1.38

Table S7. The fitting values of resistances for bare Mg||Mo_6S_8 full cells during the resting period.

Time (h)	R_s (Ω)	Error (%)	R_{ct} (Ω)	Error (%)
2	9.96	4.92	3212.00	3.72
4	10.15	1.71	3848.00	3.44
6	10.03	1.68	3768.00	3.10
8	10.18	1.74	4028.00	2.82
10	10.28	1.95	4357.00	3.37
12	10.96	1.79	4644.00	3.10

Table S8. The fitting values of resistances for Bi@Mg||Mo_6S_8 full cells during the resting period.

Time (h)	R_s (Ω)	Error (%)	R_{ct} (Ω)	Error (%)
2	10.43	1.64	272.60	3.29
4	10.42	1.74	916.10	3.59
6	10.32	1.77	1330.00	3.78
8	10.44	1.77	1881.00	3.83
10	13.00	1.78	1898.00	4.90
12	10.65	1.75	2135.00	3.87

Table S9. The fitting values of resistances for Mg||Mo_6S_8 full cells during cycling.

Cycling	R_s (Ω)	Error (%)	R_{ct} (Ω)	Error (%)
2nd	20.78	0.94	499.40	2.14
5th	20.74	0.47	180.20	1.50
10th	19.65	0.25	111.10	0.55
20th	21.30	0.34	109.70	0.87

Table S10. The fitting values of resistances for Bi@Mg||Mo_6S_8 full cells during cycling.

Cycling	R_s (Ω)	Error (%)	R_{ct} (Ω)	Error (%)
2nd	20.84	1.32	126.70	4.32
5th	19.61	0.47	85.20	2.63
10th	20.29	0.56	74.70	2.24
20th	21.21	0.58	68.79	2.04

Table S11. Electrochemical performances comparison of full cells with Mo_6S_8 cathode.

Full cell	Current density (C)	Loading (mg cm^{-2})	Cycles	Specific capacity (mAh g^{-1})	Capacity rentention (%)	CE (%)	Refs.
Mg@SnSb||Mo_6S_8	1	1.0–1.2	220	47.9	94.0	~100	5
PA-M@Mg||Mo_6S_8	0.4	2.6–3.4	400	~70	~ 64	~100	6
In/$MgCl_2$@Mg||Mo_6S_8	1	1.2	1000	66.2	~100	~100	7
Mg-Sn-Bi@Mg||Mo_6S_8	1	1.5	2400	62.3	76.2	99.9	8
Sb-Mg/$MgCl_2$@Mg||Mo_6S_8	1	1.55	1000	47.9	94.0	99.7	14
MBI@Mg||Mo_6S_8	1	/	100	29.5	71.5	~100	19
(002)-Mg||Mo_6S_8	1	1.0–1.5	1000	76	~100	~100	23
Mg@SnS_2@CC||Mo_6S_8	0.2	1.0	240	56.86	~76	98.4	24
CF-Cu@Mg||Mo_6S_8	0.5	1.59	150	60	91.1	~100	25
Bi-Mg@Mg||Mo_6S_8	1	1–1.5	1500	80	~100	~100	26
Mg@$Ni(OH)_2$@CC||Mo_6S_8	0.5	30.0	100	64.49	98.7	~100	27
Mg@ZIF_8@CC||Mo_6S_8	1	0.8–1.2	1500	65.6	90	~100	28
Bi@Mg||Mo_6S_8	1	1.0–2.0	2000	73.8	94.9	~100	**This work**

References

1 G. Kresse, *Phys. Rev. B*, 1996, 54, 11169.
2 G. Kresse, *Phys. Rev. B*, 1999, 59, 1758.
3 J. P. Perdew, *Phys. Rev. Lett.*, 1996, 77, 3865.
4 P. E. Blöchl, *Phys. Rev. B*, 1994, 50, 17953.
5 X. Peng, Y. Yuan, D. Gu, D. Li, L. Wu, L. Zhang, G. Huang, J. Wang and F. Pan, *Adv. Funct. Mater.*, 2025, 35, 2422278.
6 T. Wen, S. Tan, R. Li, X. Huang, H. Xiao, X. Teng, H. Jia, F. Xiong, G. Huang, B. Qu, J. Song, J. Wang, A. Tang and F. Pan, *ACS Nano*, 2024, 18, 11740–11752.
7 Y. Chen, X. Shen, J. Wang, Y. Zhang, Y. Hao, L. Tong, G. Huang, Q. Li, X. Zhou, B. Qu and F. Pan, *ACS Energy Lett.*, 2024, 9, 5616–5626.
8 X. Chai, H. Xie, T.-T. Zhang, Y. Xin, F. Zhang, B. He, H. Xie, L. Yu and H. Tian, *Energy Storage Mater.*, 2024, 70, 103460.
9 X. Chai, Y. Xin, B. He, F. Zhang, H. Xie and H. Tian, *Nanoscale*, 2024, 16, 9123–9135.
10 R. Zhang, *Chem. Eng. J.*, 2023, 451, 138663.
11 B. Yang, L. Xia, R. Li, G. Huang, S. Tan, Z. Wang, B. Qu, J. Wang and F. Pan, *J. Mater. Sci. Technol.*, 2023, 157, 154–162.
12 T. Wen, B. Qu, S. Tan, G. Huang, J. Song, Z. Wang, J. Wang, A. Tang and F. Pan, *Energy Storage Mater.*, 2023, 55, 816–825.
13 S. Shin, J. H. Kwak, S. H. Oh, H.-S. Kim, S.-H. Yu and H.-D. Lim, *ACS Appl. Mater. Interfaces*, 2023, 15, 28684–28691.
14 Y. Li, G. Yang, C. Zhang, W. Y. Lieu, C. Y. J. Lim, S. Sun, J. Wang, S. Jiang, Z. Xing, Z. Sofer, M.-F. Ng, W. Liu and Z. W. Seh, *Adv. Funct. Mater.*, 2022, 33, 2210639.
15 Y. Li, X. Zhou, J. Hu, Y. Zheng, M. Huang, K. Guo and C. Li, *Energy Storage Mater.*, 2022, 46, 1–9.
16 J. Zhang, X. Guan, R. Lv, D. Wang, P. Liu and J. Luo, *Energy Storage Mater.*, 2020, 26, 408–413.
17 R. Zhang, C. Cui, R. Li, Y. Li, C. Du, Y. Gao, H. Huo, Y. Ma, P. Zuo and G. Yin, *Chem. Eng. J.*, 2021, 426, 130751.
18 X. Zhou, G. Li, Y. Yu, M. Lei, K. Chen and C. Li, *Small Methods*, 2023, 8, 2301109.
19 D. Zhang, Y. Sun, X. Liu, Y. Zhang, R. Wang, Y. Zhao, M. Pan, Y. Wang, S. Chen, M. Zhou, Y. Chen, J. Yang, J. Wang and Y. NuLi, *ACS Energy Lett.*, 2024, 9, 2685–2695.
20 M. Hu, G. Li, K. Chen, X. Zhou and C. Li, *Chem. Eng. J.*, 2024, 480, 148193.
21 G. Li, K. Chen, M. Lei, T. Wang, M. Hu and C. Li, *Adv. Energy Mater.*, 2024, 14, 2401507.
22 C. Wei, L. Tan, Y. Zhang, B. Xi, S. Xiong, J. Feng and Y. Qian, *Energy Storage Mater.*, 2022, 48, 447–457.
23 J. Bi, Z. Zhou, J. Li, B. Li, X. Sun, Y. Liu, K. Wang, G. Gao, Z. Du, W. Ai and W. Huang, *Angew. Chem. Int. Ed.*, 2024, 63, e202407770.
24 F. Li, H. Dou, Z. Zhao, W. Li, Q. Bai, S. Yang and X. Wang, *Inorg. Chem. Front.*, 2025, 12, 1517–1527.
25 Y. Hao, D. Wang, Y. Chen, L. Tong, Y. Tang, G. Huang, C. Xu, Q. Li, B. Qu, F. Pan and J. Wang, *Acta Mater.*, 2025, 293, 121107.
26 J. Bi, J. Li, Z. Zhou, B. Li, K. Wang, G. Gao, Z. Du, W. Ai and W. Huang, *Adv. Mater.*, 2025, 37, 2502098.

27 G. Wang, X. Liu, H. Shi, Y. Ma, Z. Wang, C. Sun, F. Song, Z. Zhang, S. Dong, M. Sun, A. Du and G. Cui, *ACS Energy Lett.*, 2024, 9, 48–55.
28 J. Liu, M. Wang, Z. Zhang, J. Zhang, Y. He, Z. Zhou and G. Li, *J. Energy Chem.*, 2024, 90, 423–434.